

Room-Temperature Metallic Fusion-Induced Layer-by-Layer Assembly for Highly Flexible Electrode Applications

Yongkwon Song, Donghee Kim, Sungkun Kang, Younji Ko, Jongkuk Ko, June Huh, Yongmin Ko, Seung Woo Lee,* and Jinhan Cho*

To fabricate flexible electrodes, conventional silver (Ag) nanomaterials have been deposited onto flexible substrates, but the formed electrodes display limited electrical conductivity due to residual bulky organic ligands, and thus postsintering processes are required to improve the electrical conductivity. Herein, an entirely different approach is introduced to produce highly flexible electrodes with bulk metal-like electrical conductivity: the room-temperature metallic fusion of multilayered silver nanoparticles (NPs). Synthesized tetraoctylammonium thiosulfate (TOAS)-stabilized Ag NPs are deposited onto flexible substrates by layer-by-layer assembly involving a perfect ligand-exchange reaction between bulky TOAS ligands and small tris(2-aminoethyl) amine linkers. The introduced small linkers substantially reduce the separation distance between neighboring Ag NPs. This shortened interparticle distance, combined with the low cohesive energy of Ag NPs, strongly induces metallic fusion between the close-packed Ag NPs at room temperature without additional treatments, resulting in a high electrical conductivity of $\approx 1.60 \times 10^5 \text{ S cm}^{-1}$ (bulk Ag: $\approx 6.30 \times 10^5 \text{ S cm}^{-1}$). Furthermore, depositing the TOAS-Ag NPs onto cellulose papers through this approach can convert the insulating substrates into highly flexible and conductive papers that can be used as 3D current collectors for energy-storage devices.

1. Introduction

Next-generation wearable electronics with enhanced smart functions, including optoelectronics, healthcare monitoring, and flexible energy-storage/conversion devices, have become an emerging field in recent years.^[1–7] To meet the demands of this rapidly growing field, it is crucial to develop flexible electrodes that can exhibit and maintain high electrical conductivity under mechanical deformations. Therefore, many research efforts have


focused on solution-processable conductive nanomaterials that can significantly mitigate the impact of external mechanical stimuli by minimizing the contact area with the substrates.^[8–10] In particular, silver (Ag) nanomaterials are considered as one of the most promising candidates for flexible electrodes because of their superior electrical conductivity and low price compared to other conductive metals, such as gold (Au) or platinum. In most cases, Ag nanomaterials, including nanoparticles (NPs) and high-aspect-ratio nanowires (NWs), stabilized by bulky organic ligands (e.g., oleic acid, trioctylamine, poly(acrylic acid) (PAA), or poly(vinyl pyrrolidone)) have mainly been used as the conductive components to prepare flexible electrodes using solution processes (i.e., Meyer rod coating, spin-coating, or printing).^[11–24] However, these approaches generally impart the high contact resistance between Ag components due to the presence of residual bulky ligands or polymers bound to the metal surface. Thus, the conventional solution processes require various subsequent sintering processes, such as thermal annealing (>200 °C), mechanical welding, chemical treatments by electrolyte (or sintering agent), plasma/microwave treatments (particularly, the microwave treatment onto Ag NP-coated films can generate an electric spark), to form a conductive Ag solid.^[18–25] For an example, in the case of PAA-stabilized Ag NP inks, it should be noted that the thermal decomposition of PAA stabilizers occurs above 200 °C. Therefore, the electrical conductivity of Ag ink-based film can be significantly increased after sufficient decomposition or removal of bulky insulating PAA. Furthermore, the above-mentioned approaches based mainly on spin-coating or inkjet printing methods have limitations in accurately controlling the loading amount of metal components and applications depending on the mechanical, chemical, and/or thermal properties of substrates. More specifically, those methods cannot effectively coat the interior surface of 3D porous substrates with Ag NPs due to the intrinsic restrictions of processes and the use of highly concentrated and viscous Ag NP solution.

A recent study using high-resolution transmission electron microscopy (HR-TEM) showed that Ag NPs stabilized with anionic citrate ion ligands in water could behave as soft matter that wetted the surface of gold nanorods without additional

Y. Song, Dr. D. Kim, S. Kang, Y. Ko, Dr. J. Ko, Prof. J. Huh, Dr. Y. Ko, Prof. J. Cho

Department of Chemical and Biological Engineering
Korea University
145 Anam-ro, Seongbuk-gu, Seoul 02841, Republic of Korea
E-mail: jinhan71@korea.ac.kr

Dr. Y. Ko, Prof. S. W. Lee
School of Mechanical Engineering
Georgia Institute of Technology
Atlanta, GA 30332-0245, USA
E-mail: seung.lee@me.gatech.edu

 The ORCID identification number(s) for the author(s) of this article can be found under <https://doi.org/10.1002/adfm.201806584>.

DOI: 10.1002/adfm.201806584

treatments at room temperature because of the low cohesive energy of Ag (2.95 eV per Ag atom; 3.81 eV per Au atom).^[26] Additionally, the metallic bonding between Ag NPs with an interparticle separation distance of less than 5 Å has been reported.^[27,28] Although the occurrence of such metallic wetting and bonding of Ag NPs without additional treatments can contribute to the formation of conductive Ag solids, these phenomena were mainly observed in the nanoscale region, and did not extend to the practical preparation of conductive films. On the other hand, the electrical conductivity of Ag NP-based films, which strongly depends on the interparticle distance in large scale, are affected by the presence of bulky ligands and the packing density of the Ag NPs. Thus, if the distance between neighboring Ag NPs can be controlled through interfacial engineering, it can induce the metallic fusion of Ag NPs at room temperature during the assembly process, substantially increasing the electrical conductivity without the need for any subsequent treatment.

Along with the preparation of conductive films, significant attention has been paid to flexible substrates that act as bases for conductive nanomaterials. Among the variety of flexible substrates, highly porous cellulose papers are considered promising substrates for next-generation flexible electrodes due to their large specific surface area, good mechanical properties, light weight, and low cost. Therefore, many studies have concentrated on coating paper substrates with conductive nanomaterials without disturbing their native superior properties.^[29–35] For example, paper electrodes have been easily prepared by the incorporation of carbon nanotubes (CNTs), reduced graphene oxides, and/or Ag nanomaterials into papers using the soaking processes, the vacuum filtration, or the Meyer rod coating.^[11,31–35] However, these solution processes also have limitations in controlling the loading amount and uniformity of the conductive nanomaterials because of the highly porous structure of paper substrates. Furthermore, the unfavorable interfacial interaction between conductive nanomaterials and paper substrates results in the low packing density of conductive components and unstable mechanical properties, which are major obstacles to the formation of highly conductive and robust large-area paper electrodes.

Layer-by-layer (LbL) assembly using complementary interactions enables the fabrication of multilayered nanocomposites with tailored thickness (or loading amount), composition, and functionalities under mild conditions irrespective of substrate size or shape.^[36–50] Traditional electrostatic LbL assembly of electrodes often involves pairing charged polymers (i.e., polyelectrolytes, PEs) with oppositely charged metal NPs (mainly citrate ion-stabilized metal NPs) in water.^[47–49] However, the polymer linkers that bridge neighboring metal NPs increase the contact resistance between metal NPs, which results in the low electrical conductivity of the electrodes. Additionally, the long-range electrostatic interparticle repulsion limits the loading amount of charged metal NPs and increases the interparticle distance between adjacent metal NPs (packing density <30%), consequently increasing the contact resistance.^[2,49] Moreover, if charged metal NPs are deposited onto porous paper substrates using oppositely charged polymer linkers in water, the consecutive deposition of polymers can gradually block the substrate pores.^[50]

Herein, we report the assembly of highly porous, flexible, and conductive Ag NP-coated paper electrodes using the room-temperature metallic fusion, which can produce 3D current collectors for flexible/wearable energy-storage electrodes. This unique metallic fusion process involves the LbL assembly of the newly synthesized tetraoctylammonium thiosulfate (TOAS)-stabilized Ag NPs (TOAS-Ag NPs) and the small-molecule linkers (tris(2-aminoethyl)amine (TAA, $M_w \approx 146$) in organic media without electrostatic repulsion between NPs. These TOAS ligands can also be used to synthesize a variety of metal NPs such as Au and Cu NPs. During the LbL process, almost perfect ligand-exchange reaction between the bulky/insulating TOAS ligands loosely bound to the Ag NP surface and the small TAA molecules dramatically decreased the interparticle distance, which induced metallic fusion of the Ag NPs (**Figure 1**). The separation distance between TAA-coated Ag NPs computed by atomistic molecular dynamics (MD) simulations was ≈ 6 Å, which was slightly above the threshold distance (≈ 5 Å) for the formation of metallic bonding reported by other research groups.^[27,28] The closely packed Ag NPs with minimized interparticle separation distance became mutually diffusive at room temperature without additional treatments. The obtained (TOAS-Ag NP/TAA)₂₀ multilayers exhibited a bulk metal-like electrical conductivity of $\approx 1.60 \times 10^5$ S cm⁻¹ ($\approx 25.4\%$ of bulk Ag conductivity $\approx 6.30 \times 10^5$ S cm⁻¹), and when applying additional thermal treatment (160 °C), the electrical conductivity was enhanced up to 4.62×10^5 S cm⁻¹ (67.6% of bulk Ag conductivity), outperforming the existing Ag NP-based films.

Although oleic acid (OA)-stabilized Ag NPs (OA-Ag NPs) can also be densely packed and LbL-assembled with TAA molecules through the above-mentioned same ligand-exchange reaction, it should be noted that the resulting (OA-Ag NP/TAA)_n multilayers display an insulating property without the metallic fusion phenomena because of the remaining bulky OA ligands caused by the low degree of ligand-exchange reaction between OA ligands and TAA molecules during LbL assembly. Furthermore, the presence of bulky organics between vertically adjacent Ag NPs can explain why the high electrical conductivity is difficult to be achieved from the traditional LbL-assembled (charge metal NP/oppositely charged polymer linker)_n multilayers and the highly viscous Ag NP inks containing polymer stabilizers and/or binders as well as (OA-Ag NP/TAA)_n films without additional treatments. On the other hand, our approach based on the small molecule linker-induced ligand-exchange reaction allows a dramatic increase in electrical conductivity by providing the metallic fusion effects at room temperature (**Figure 1**; **Figure S1**, Supporting Information).

Based on this unique LbL assembly involving metallic fusion, we also demonstrate that the consecutive deposition of TOAS-Ag NPs onto cellulose papers can convert the insulating substrates into porous metallic papers by uniformly coating over the entire surface area ranging from the interior to the exterior. Furthermore, the subsequent deposition of high-energy pseudocapacitive OA-stabilized Fe₃O₄ NPs (OA-Fe₃O₄ NPs) onto these metallic papers can produce flexible energy-storage electrodes. These flexible electrodes maintained a high degree of mechanic flexibility similar to that of their pristine papers and exhibited high areal capacitances due to their highly porous structure. We believe that our approach can provide an

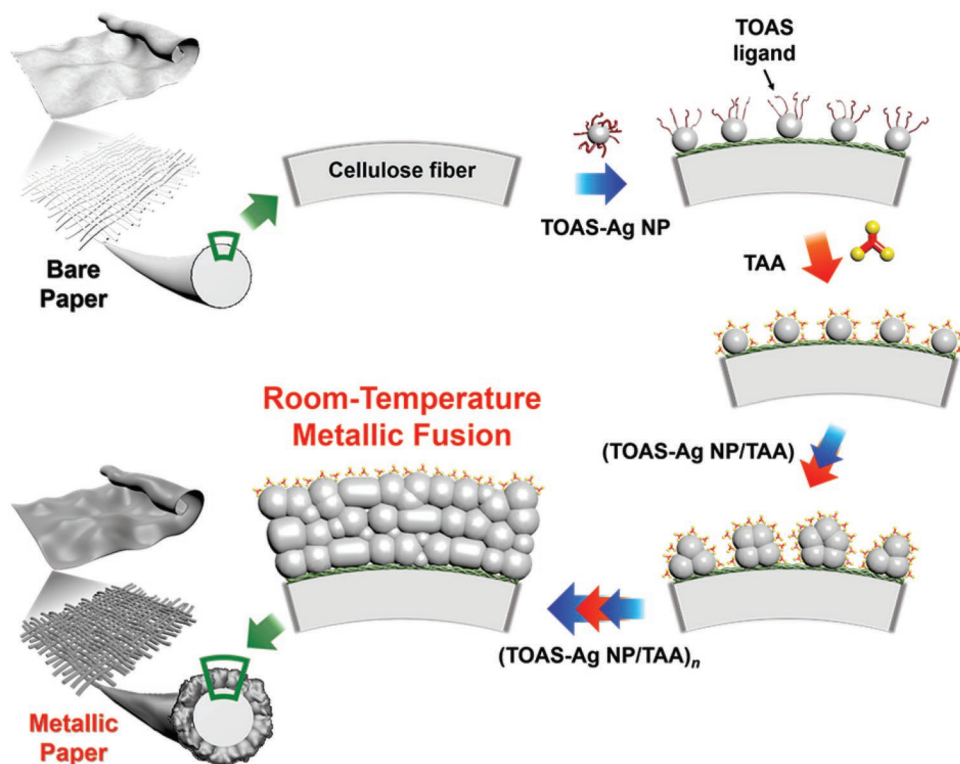


Figure 1. Schematic illustration of the formation of $(\text{TOAS-Ag NP/TAA})_n$ multilayers on paper by room-temperature metallic fusion during perfect ligand-exchange LbL assembly.

important basis for developing flexible electrodes in a variety of other energy applications, such as energy-storage/conversion devices, sensors, actuators, and fuel cells, requiring a high electrical conductivity and large surface area.

2. Results and Discussion

To obtain the stable dispersion of Ag NPs needed to facilitate a perfect ligand-exchange reaction with organic linkers in organic media, we prepared TOAS-Ag NPs in toluene by the modified Brust-Schiffrin method.^[51,52] When sodium thiosulfate ($\text{Na}_2\text{S}_2\text{O}_3$) was added to a reaction mixture containing precursor silver ions (Ag^+), dithiosulfatoargentate(I) anions ($[\text{Ag}(\text{S}_2\text{O}_3)_2]^{3-}$) complexed with tetraoctylammonium (TOAS-Ag^+) were formed in the toluene phase, as confirmed in ^1H NMR spectra (Figure S2, Supporting Information),^[53] and subsequent reduction by sodium borohydride (NaBH_4) produced a highly stable TOAS-Ag NP dispersion in toluene (Figure 2a). The synthesized TOAS-Ag NPs showed a uniform size of ≈ 8.3 nm in diameter with a well-defined crystal structure (Figure 2b; Figure S3a–c, Supporting Information). Additionally, the TOAS-Ag NPs maintained a good dispersion in toluene without aggregation even after one month, representing their high colloidal stability (Figure S3d, Supporting Information). Considering that the Ag NPs stabilized with conventional tetraoctylammonium bromide (TOABr) ligands exhibit unsatisfactory long-term stability (a few hours),^[54] the enhanced stability of TOAS-Ag NPs is due to the presence of thiosulfate counter anions, which

interact more strongly with the metal NP surface than bromide anions.^[52] We also confirmed that these TOAS ligands can be employed to synthesize other metal NPs such as gold and copper (Cu) NPs (Figure S4, Supporting Information).

The synthesized TOAS-Ag NPs were LbL-assembled with TAA molecules by the perfect ligand-exchange reaction between the TOAS ligands loosely bound to the Ag NP surface and the NH_2 groups of the TAA molecules. This ligand-exchange reaction was examined as a function of bilayer number (n) using Fourier transform infrared (FTIR) spectroscopy (Figure 2c; Figure S5, Supporting Information). Specifically, the absorption peaks corresponding to C–H stretching ($\approx 2850\text{--}2950\text{ cm}^{-1}$) of the TOAS alkyl chains appeared after submerging the poly(ethylenimine) (PEI)-coated substrate into a toluene solution of dispersed TOAS-Ag NPs, which was consistent with the deposition of the TOAS-Ag NP layer ($n = 0.5$). These characteristic peaks of the TOAS ligands disappeared completely after submerging the TOAS-Ag NP layer-coated substrate into an ethanol solution of dissolved TAA ($n = 1$), indicating that the TOAS ligands attached to the Ag NP surface were eliminated entirely. Considering that the NH_2 groups of TAA molecules, with their lone pair of electrons, have a higher affinity for the metal surface than the ammonium groups of TOAS ligands, these observations in the FTIR spectra imply that TAA molecules are directly adsorbed onto the Ag NP surface through the perfect ligand-exchange reaction with TOAS ligands. This trend recurred with increasing bilayer number and represented the successful LbL assembly of $(\text{TOAS-Ag NP/TAA})_n$ multilayers. As a result, the organic linker bridging adjacent Ag NPs consisted of only one small

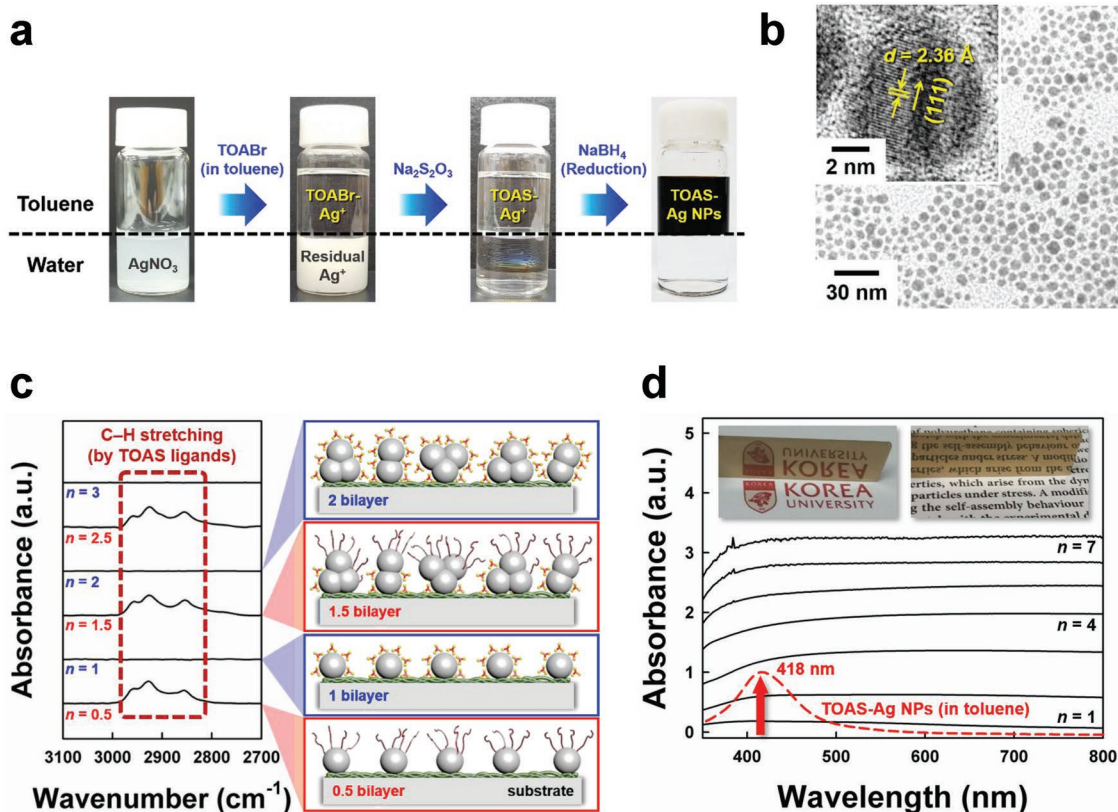


Figure 2. a) Synthetic process of TOAS–Ag NPs dispersed in toluene. b) HR-TEM images of TOAS–Ag NPs. The inset shows that the TOAS–Ag NPs have a well-defined crystal structure with a lattice spacing (d) of 2.36 Å. c) FTIR spectra and schematic representation of LbL-assembled (TOAS–Ag NP/TAA) $_n$ multilayers as a function of bilayer number (n), exhibiting the perfect ligand-exchange reaction. d) UV–vis absorbance spectra of (TOAS–Ag NP/TAA) $_n$ multilayers on a quartz substrate as a function of bilayer number. UV–vis absorbance spectra of TOAS–Ag NPs in toluene (red dashed line, arbitrary unit) are also shown for comparison. The inset displays the reflective property of the (TOAS–Ag NP/TAA) $_7$ multilayer-coated quartz substrate.

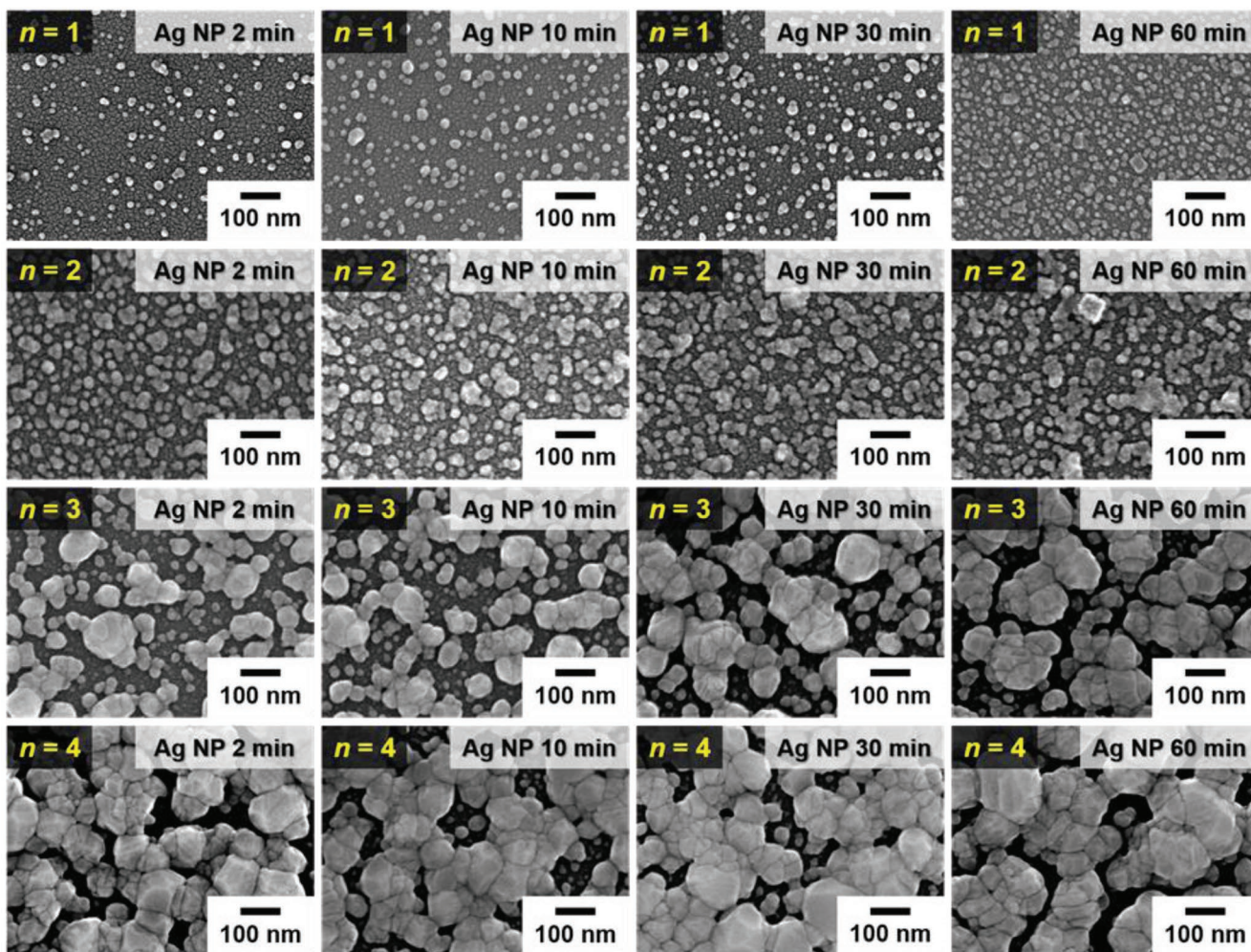
TAA molecule ($M_w \approx 146$), which significantly decreased the distance between neighboring Ag NPs and consequently induced the metallic fusion of Ag NPs with minimized interparticle distance. We also monitored the optical properties of LbL-assembled (TOAS–Ag NP/TAA) $_n$ multilayers with increasing bilayer number by UV–vis spectroscopy (Figure 2d). The characteristic surface plasmon peak of TOAS–Ag NPs dispersed in toluene (at 418 nm, red dashed line in Figure 2d) completely disappeared after the deposition of two bilayers, which shows an absorbance behavior similar to that of Ag-sputtered film (Figure S6, Supporting Information). These results suggest that the interparticle distance of adjacent Ag NPs decreases remarkably in both the lateral and vertical directions.

Building on these results, we further investigated the surface morphology of LbL-assembled (TOAS–Ag NP/TAA) $_n$ multilayers with increasing bilayer number and TOAS–Ag NP deposition time by field-emission scanning electron microscopy (FE-SEM; Figure 3a). Interestingly, larger Ag particles, created by fusing small TOAS–Ag NPs into large Ag particles, were observed as the bilayer number increased. This phenomenon is similar to Ostwald ripening, in which small particles are incorporated into larger particles.^[25] Longer deposition times for the TOAS–Ag NP layer also resulted in the slight growth of the Ag NPs, but this effect was not as pronounced as for the bilayer number. With the formation of three bilayers

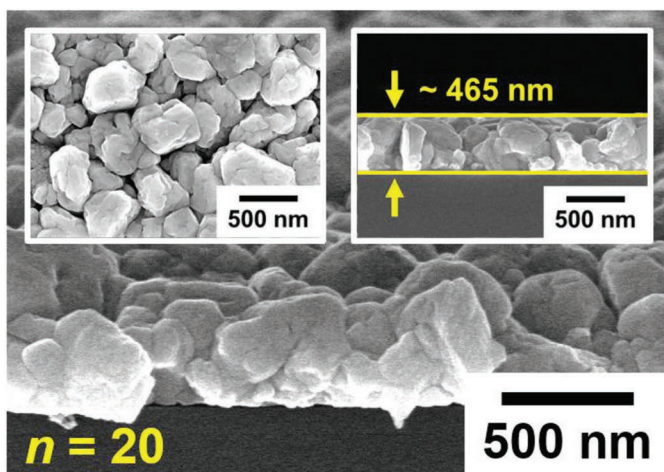
(i.e., (TOAS–Ag NP/TAA) $_3$ multilayers), the fused Ag particles with a few hundred nanometers in size started to interconnect, and individual nonfused TOAS–Ag NPs were hardly detected by FE-SEM. When the bilayer number increased from 5 to 20, the total film thickness increased substantially from ≈ 83 to 465 nm (Figure 3b,c; Figure S7, Supporting Information). The average bilayer thickness of the (TOAS–Ag NP/TAA) $_{20}$ multilayers was 23.3 nm, which exceeded the diameter of the TOAS–Ag NPs (8.3 nm). This difference is caused by the metallic fusion of densely packed Ag NPs within (TOAS–Ag NP/TAA) $_n$ multilayers, which allows the bilayer to be thicker than the initial size of the TOAS–Ag NPs, but in a controlled manner, as shown in Figure 3c. In contrast, for (inorganic NP/polymer) $_n$ multilayers fabricated by traditional electrostatic LbL assembly in water, the average bilayer thickness did not reach the diameter of the NPs because of the insufficient deposition of NPs due to the long-range electrostatic repulsion between the same charged NPs.^[49] Here, it should be noted that the fused structure of the (TOAS–Ag NP/TAA) $_n$ multilayers is obtained by the perfect ligand-exchange reaction between the bulky TOAS ligands and the small TAA linkers, which can minimize the interparticle separation distance between neighboring Ag NPs.

To confirm our hypothesized mechanism, we prepared OA–Ag NPs ≈ 6.5 nm in diameter in toluene (Figure 4a), and then,

a



b



c

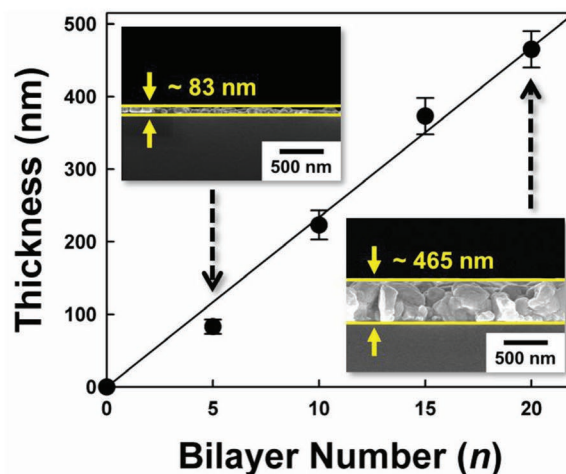


Figure 3. a) Planar FE-SEM images of $(\text{TOAS-Ag NP/TAA})_n$ multilayers as a function of bilayer number and TOAS-Ag NP deposition time. b) Tilted (main image), planar (top right inset), and cross-sectional (top left inset) FE-SEM images of the $(\text{TOAS-Ag NP/TAA})_{20}$ multilayers. c) Film thickness of the $(\text{TOAS-Ag NP/TAA})_n$ multilayers as a function of bilayer number ($n = 5, 10, 15,$ and 20).

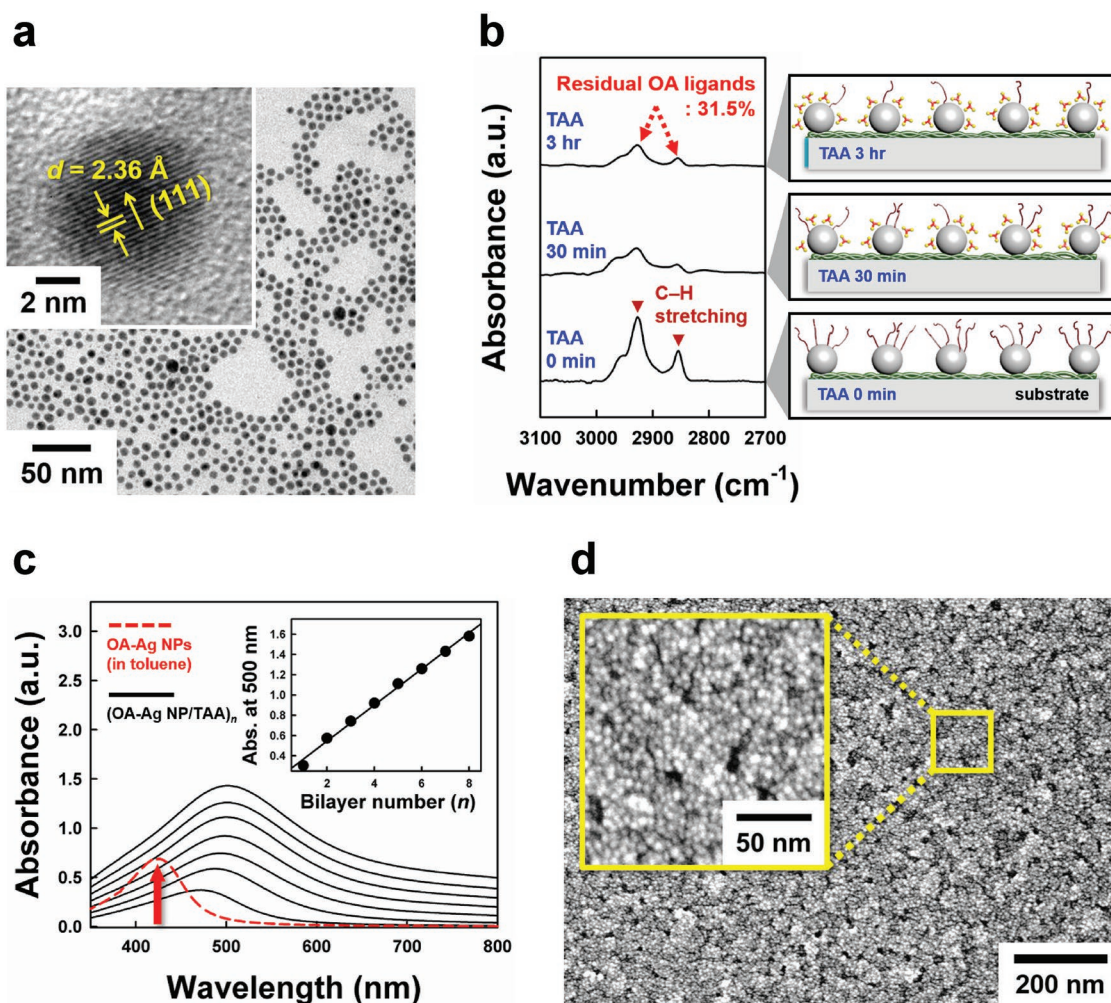


Figure 4. a) HR-TEM images of OA-Ag NPs with a lattice spacing of 2.36 Å. b) Time-dependent FTIR spectra of the partial ligand-exchange reaction during the deposition of TAA onto the OA-Ag NP layer-coated substrate. c) UV-vis absorbance spectra of $(\text{OA-Ag NP/TAA})_n$ multilayers on a quartz substrate with increasing bilayer number. The red dashed line shows the UV-vis absorbance spectra of OA-Ag NPs dispersed in toluene (arbitrary unit) and the inset exhibits the absorbance of $(\text{OA-Ag NP/TAA})_n$ multilayers at 500 nm as a function of bilayer number. d) Planar FE-SEM images of the $(\text{OA-Ag NP/TAA})_{20}$ multilayers.

these NPs were LbL-assembled with TAA molecules by a ligand-exchange reaction using the same experimental conditions as those used in the formation of $(\text{TOAS-Ag NP/TAA})_n$ multilayers. As shown in the FTIR spectra (Figure 4b; Figure S5, Supporting Information), the C-H stretching peaks ($\approx 2850\text{--}2950 \text{ cm}^{-1}$) derived from the long alkyl chains of the OA ligands were still present, although the outermost OA-Ag NP layer-coated substrate was sufficiently submerged into an ethanol solution of TAA for 3 h. This phenomenon considerably conflicts with the previous disappearance of the absorbance peaks of the TOAS ligands within 20 min. Consequently, the degree of ligand-exchange reaction was estimated to be $\approx 68.5\%$ based on the area of the absorbance peaks. Additionally, the UV-vis absorbance spectra of the $(\text{OA-Ag NP/TAA})_n$ multilayers exhibited an evident surface plasmon peak at 500 nm with a slight redshift despite the increase in bilayer number (Figure 4c). These observations imply that the separation distance between adjacent Ag NPs is almost constant, but not close, due to the residual OA ligands. Therefore, the $(\text{OA-Ag NP/TAA})_{20}$ multilayers

preserved the pristine size and shape of the OA-Ag NPs without any merged structure, as shown in the FE-SEM images (Figure 4d), which is in stark contrast with the $(\text{TOAS-Ag NP/TAA})_{20}$ multilayers. These results strongly support that the separation distance between neighboring Ag NPs is significantly influenced by the degree of ligand-exchange reaction, which operates as a critical factor for controlling the structural and optical properties of LbL-assembled nanocomposites.

The separation distance between adjacent TAA-coated Ag NPs in the $(\text{TOAS-Ag NP/TAA})_n$ multilayers was calculated using atomistic MD simulations. When the ratio of the surface area of the Ag NPs to that covered by TAA molecules ($S_{\text{TAA}}/S_{\text{Ag}}$) was assumed to be around unity, the separation distance was estimated to be $\approx 6 \text{ \AA}$ (Figure 5a), slightly exceeding the reported threshold distance ($\approx 5 \text{ \AA}$) for the metallic fusion of Ag NPs.^[27,28] This minimized interparticle distance between neighboring Ag NPs with low cohesive energy (2.95 eV per atom) facilitates mutual atom diffusion within the assembled TOAS-Ag NPs (more specifically, Ag NPs separated by one TAA molecule). In

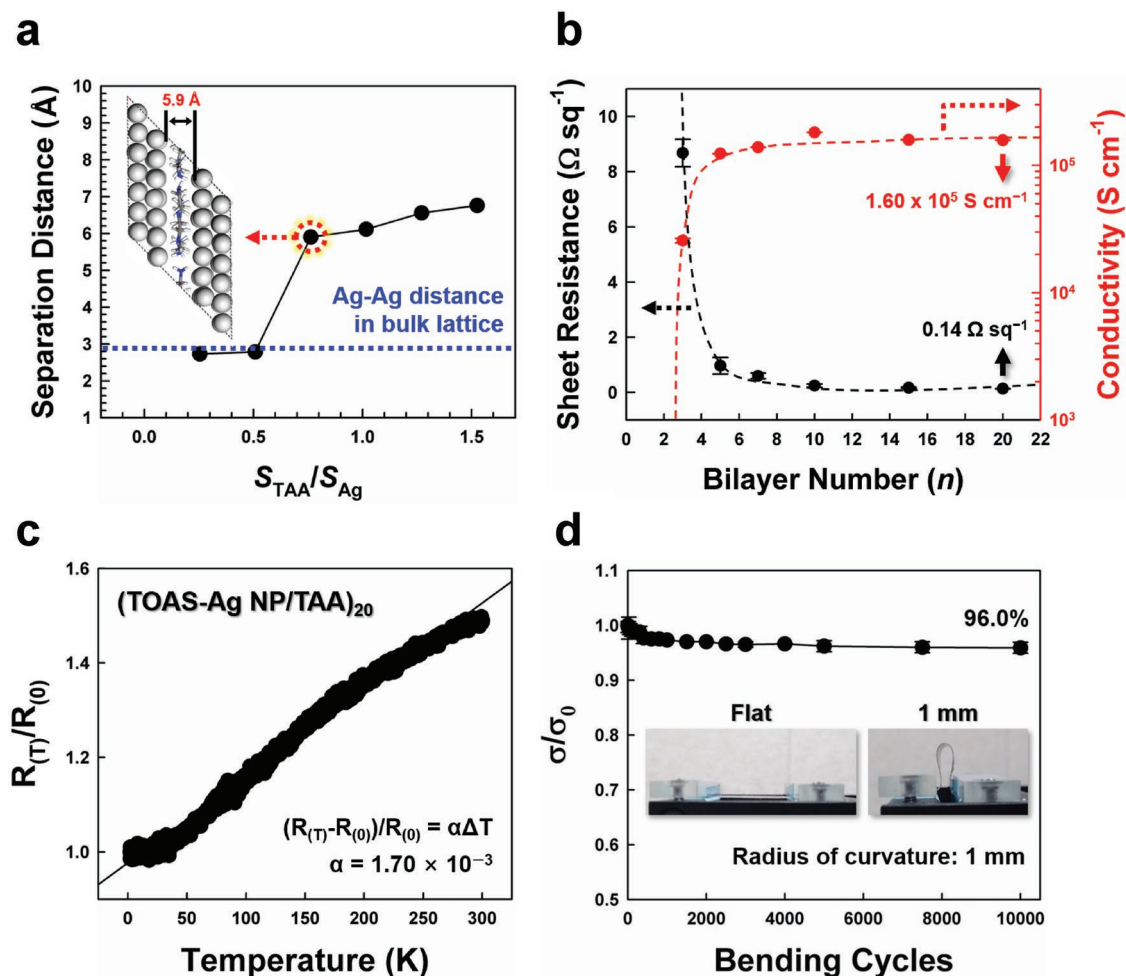


Figure 5. a) Atomistic MD-computed minimal distance between Ag atomic surfaces separated by TAA molecules as a function of surface coverage ratio (S_{TAA}/S_{Ag}), where S_{TAA} and S_{Ag} are the surface area covered by TAA molecules and the surface area of the Ag atomic layers, respectively. The blue dashed line represents the Ag–Ag distance in the bulk lattice (≈ 2.89 Å). The inset shows the simulated molecular structure of TAA molecules between the Ag atomic surfaces at $S_{TAA}/S_{Ag} = 0.76$. b) Sheet resistance and electrical conductivity of $(TOAS-Ag NP/TAA)_n$ multilayers on Si wafers as a function of bilayer number. c) Change in the resistance ($R_{(T)}/R_{(0)}$) of the $(TOAS-Ag NP/TAA)_{20}$ multilayers on a Si wafer as the temperature is decreased from 300 to 2 K. d) Change in the electrical conductivity (σ/σ_0) of the $(TOAS-Ag NP/TAA)_{10}$ multilayer-coated PET substrate as a function of bending cycles (curvature radius: 1 mm), where σ_0 is the electrical conductivity at the initial state.

turn, the metallic fusion of multilayered Ag NPs can be readily triggered by small perturbations, such as the fluctuation-induced transient exposure of the bare Ag NP surface, even at room temperature. Additionally, the room-temperature metallic fusion is predicted to significantly decrease the contact resistance between Ag components by increasing the contact points in the Ag NP arrays. The sheet resistance of the $(TOAS-Ag NP/TAA)_n$ multilayers dramatically decreased from $>10^8$ to $1 \Omega \text{ sq}^{-1}$ (electrical conductivity $\approx 1.23 \times 10^5 \text{ S cm}^{-1}$) when the bilayer number was increased from 2 to 5 (Figure 5b). This remarkable change in the electrical conductivity obtained from room temperature process can also be predicted from the surface morphology of the $(TOAS-Ag NP/TAA)_n$ multilayers, as shown in Figure 3a. When the bilayer number was increased from 2 to 3 (see the FE-SEM images referred to as “Ag NP 60 min”), the fused Ag NPs were clearly interconnected. Therefore, three bilayers ($n = 3$) could be considered the onset point (i.e., percolation threshold) for the formation of conductive networks

in the $(TOAS-Ag NP/TAA)_n$ multilayers. The $(TOAS-Ag NP/TAA)_{20}$ multilayers with highly interconnected structures exhibited an extremely low sheet resistance ($0.14 \Omega \text{ sq}^{-1}$) and a high electrical conductivity ($1.60 \times 10^5 \text{ S cm}^{-1}$). Furthermore, it should be noted that an additional heat treatment can improve the electrical conductivity of $(TOAS-Ag NP/TAA)_{20}$ multilayers up to $4.26 \times 10^5 \text{ S cm}^{-1}$ at an annealing temperature of 160°C , which is superior to previously reported Ag NP-based films (Figure S8 and Table S1, Supporting Information). On the other hand, $(OA-Ag NP/TAA)_{20}$ multilayers without merged structures exhibited an electrically insulating property ($>10^8 \Omega \text{ sq}^{-1}$), suggesting that the long alkyl chains of the remaining OA ligands seriously limited electron transfer between adjacent OA–Ag NPs.

We also confirmed that the electron-transfer mechanism of the $(TOAS-Ag NP/TAA)_{20}$ multilayers followed the temperature-dependent electrical conductivity equation used to describe the metallic conduction behavior (i.e., $\Delta R/R_0 = \alpha \Delta T$,

where R and α are the resistance (Ω) and the temperature coefficient, respectively) instead of tunneling (or hopping) conduction behavior (i.e., the equation for semiconducting kinetics is $\sigma = \sigma_0 \exp(-A/T^{1/d+1})$ for a variable-range tunneling ($d = 1$) or hopping ($d = 3$) mechanism, where σ is the conductivity, T is the absolute temperature (K), A is a constant, and d is the dimensionality; Figure 5c; Figure S9, Supporting Information).^[2] More specifically, with decreasing the temperature from 300 to 2 K, the electrical resistivity of the (TOAS–Ag NP/TAA)₂₀ multilayers gradually decreased, whereas their electrical conductivity increased, indicating typical metallic behavior. The (TOAS–Ag NP/TAA)₂₀ multilayers exhibited a positive temperature coefficient of $1.7 \times 10^{-3} \text{ K}^{-1}$, calculated by the equation for metallic conduction behavior. To evaluate the mechanical stability of the LbL-assembled multilayers, we deposited (TOAS–Ag NP/TAA)₁₀ multilayers onto poly(ethylene terephthalate) (PET) substrates and investigated their electrical conductivity under repetitive mechanical stress (or strain). Even under high mechanical stimulus during repeated bending cycles and curvature tests, the prepared flexible electrodes consistently maintained a high electrical conductivity (Figure 5d; Figure S10, Supporting Information). They retained 96.0% of their initial electrical conductivity ($\sigma_0 \approx 1.30 \times 10^5 \text{ S cm}^{-1}$) after 10 000 bending cycles. These results imply that the (TOAS–Ag NP/TAA)_n multilayers can effectively offset the impact of external mechanical stimuli, making them promising flexible electrodes.

Based on these results, we prepared highly porous Ag NP-coated papers that can be used as 3D current collectors with large surface areas. To this end, (TOAS–Ag NP/TAA)_n multilayers were deposited onto cellulose papers (Korean Hanji), successfully converting the insulating substrates to metallic conductive papers (MCPs). FE-SEM and energy dispersive X-ray spectroscopy (EDX) images of the (TOAS–Ag NP/TAA)₃₀ multilayer-coated paper showed that the entire surface area of the paper, ranging from the interior to the exterior, was uniformly and densely coated by Ag NPs without notably changing its native porous structure (Figure 6a). More importantly, the 104 μm thick MCP exhibited an extremely low sheet resistance of $0.31 \Omega \text{ sq}^{-1}$ and a high electrical conductivity of 308 S cm^{-1} , despite a relatively low density of 0.41 g cm^{-3} (for comparison, the density of pristine paper is 0.29 g cm^{-3}) (Figure 6b). Additionally, our approach, metallic fusion LbL assembly, can be applied to various types of substrates irrespective of shape or size. For example, depositing (TOAS–Ag NP/TAA)_n multilayers onto Kirigami-structured paper produced a conductor that could be mechanically increased up to 250% without a decrease in the electrical conductivity (Figure 6c). Large-area Ag NP-coated paper ($15 \text{ cm} \times 15 \text{ cm}$) was also prepared and maintained its electrical conductivity even after repeated exposure to mechanical stimuli, such as crumpling and unfolding (Figure 6d). Moreover, flexible electrodes based on various substrates, including cellulose paper, polyester textile, cotton textile, and cotton thread, were fabricated by depositing (TOAS–Ag NP/TAA)_n multilayers and displayed metallic conductive behavior (Figure S11, Supporting Information).

The prepared MCPs (i.e., (TOAS–Ag NP/TAA)₃₀ multilayer-coated papers) were utilized as 3D current collectors for flexible energy-storage electrodes. To produce a model system,

the high-energy pseudocapacitive OA–Fe₃O₄ NPs were successively deposited with TAA molecules on the MCPs through a partial ligand-exchange reaction, which resulted from the higher affinity of the TAA molecules for the Fe₃O₄ NP surface compared to the OA ligands (Figure S12, Supporting Information). In this case, TAA molecules directly bridged the cellulose fiber/Ag NP/Fe₃O₄ NP interfaces and enabled the fabrication of highly integrated flexible energy-storage electrodes without blocking the porous structure of the MCPs (Figure S13, Supporting Information). The mass loading of (OA–Fe₃O₄ NP/TAA)_m multilayers on the MCPs increased linearly with bilayer number (m) and was ≈ 25 times higher than that of (OA–Fe₃O₄ NP/TAA)_m multilayers on nonporous Ag substrates (Ag foils) (Figure 7a). These observations suggest that the areal capacity of energy-storage electrodes can be greatly enhanced by using porous MCPs and controlled by tuning the layer number of high-energy pseudocapacitive OA–Fe₃O₄ NPs.

The charge-storage performance of (OA–Fe₃O₄ NP/TAA)_m multilayer-coated MCP electrodes (Fe₃O₄-MCP electrodes) was investigated in a three-electrode cell configuration using $0.5 \text{ M Na}_2\text{SO}_3$ as an electrolyte. Cyclic voltammetry (CV) measurements of the Fe₃O₄-MCP electrodes were conducted at a scan rate of 5 mV s^{-1} (Figure S14a, Supporting Information), and their corresponding areal and specific capacitances were evaluated as a function of the OA–Fe₃O₄ NP mass loading (Figure 7b). The asymmetric CV curves exhibited the characteristic redox peaks of Fe₃O₄ NPs (i.e., the redox reaction of sulfur in the form of sulfate and sulfite anions on the surface of the Fe₃O₄ NPs and the redox reaction between Fe(II) and Fe(III) in the electrolyte solution),^[55] and the current density and areal capacitance gradually improved with increasing mass loading or bilayer number. The areal capacitance of the Fe₃O₄-MCP electrodes increased from 102 to 212 mF cm^{-2} when the OA–Fe₃O₄ NP mass loading was increased from 0.40 to 0.80 mg cm^{-2} . However, as mentioned above, the OA–Fe₃O₄ NP mass loading and the areal capacitance in our system can be further scaled by increasing the bilayer number, although the specific capacitance will gradually decrease due to the increased internal resistance of the electrodes (Figure S14b, Supporting Information).

We also assessed the impact of the porous substrate on the areal capacitances by comparing Fe₃O₄-MCP electrodes and (OA–Fe₃O₄ NP/TAA)_m multilayer-coated Ag foil electrodes (Fe₃O₄-nonporous Ag electrodes). As shown in Figure 7c, the current response of the Fe₃O₄-MCP electrode was remarkably higher than that of the Fe₃O₄-nonporous Ag electrode at the same bilayer number ($m = 20$). Corresponding to the current response, the Fe₃O₄-MCP electrode displayed a high areal capacitance of 212 mF cm^{-2} at a scan rate of 5 mV s^{-1} , in stark contrast to the value obtained for the Fe₃O₄-nonporous Ag electrode (20 mF cm^{-2}). At other bilayer numbers ($m = 10$ and 15 ; Figure S14c, Supporting Information), the areal capacitance displayed similar trends. In addition, the Fe₃O₄-MCP electrodes with a mass loading of 0.88 mg cm^{-2} exhibited good pseudocapacitive behavior in the CV curves for scan rates ranging from 5 to 200 mV s^{-1} (Figure S14d, Supporting Information) and in the galvanostatic charge/discharge (GCD) curves for current densities ranging from 1 to 5 mA cm^{-2} (Figure S14e, Supporting Information). This superior electrochemical performance

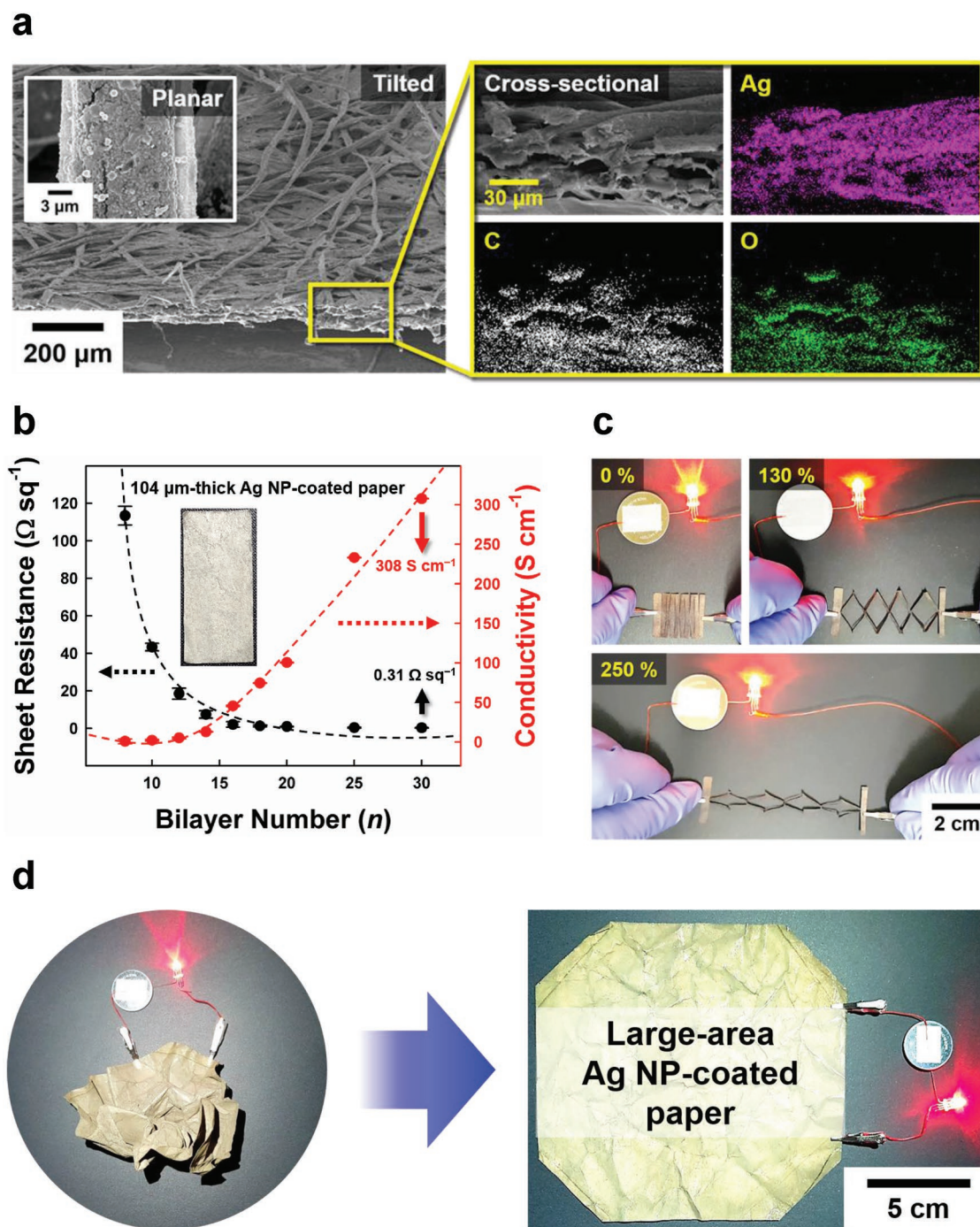


Figure 6. a) Planar, tilted, and cross-sectional FE-SEM images and EDX images of $(\text{TOAS-Ag NP/TAA})_{30}$ multilayers on cellulose paper. b) Sheet resistance and electrical conductivity of the $(\text{TOAS-Ag NP/TAA})_n$ multilayer-coated papers ($104 \mu\text{m}$ thickness) as a function of bilayer number. The inset shows a photograph of the $(\text{TOAS-Ag NP/TAA})_{30}$ multilayer-coated paper. c) Photographic images of stretchable $(\text{TOAS-Ag NP/TAA})_{30}$ multilayer-coated paper with a Kirigami structure under various strain conditions. d) Photographic images of large-area Ag NP-coated paper ($15 \text{ cm} \times 15 \text{ cm}$). The red LED remained on even after repetitive crumpling and unfolding.

mainly originates from the large surface area of the highly porous electrodes, which is closely related to the OA- Fe_3O_4 NP mass loading. The Fe_3O_4 -MCP electrodes with a mass loading of 0.88 mg cm^{-2} maintained 96.7% of their initial capacitance after 5000 CV cycles at a scan rate of 100 mV s^{-1} (Figure 7d), which indicates stable adsorption of the NPs.

3. Conclusion

We demonstrated that highly flexible paper with metal-like electrical conductivity can be prepared by the room-temperature metallic fusion of LbL-assembled Ag NPs. Specifically, the loosely bound, bulky TOAS ligands on the Ag NP surface

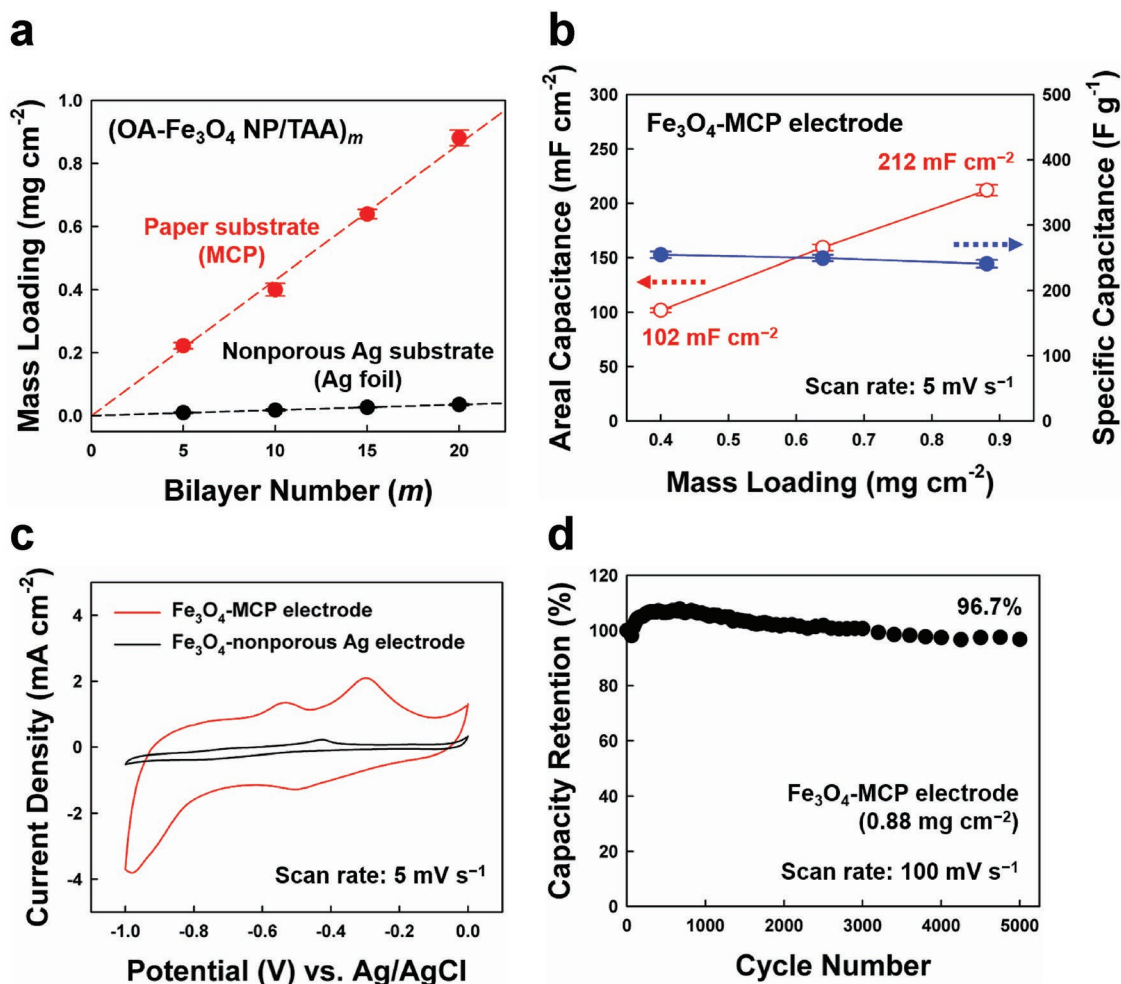


Figure 7. a) Mass loading of $(\text{OA-Fe}_3\text{O}_4 \text{ NP/TAA})_m$ multilayers on porous paper substrates (MCPs) and nonporous Ag substrates (Ag foils) as a function of bilayer number (m). b) Areal and specific capacitances of Fe_3O_4 -MCP electrodes as a function of $\text{OA-Fe}_3\text{O}_4$ NP mass loading. A mass loading increases from 0.40 to 0.88 mg cm^{-2} , which corresponds to the increase of bilayer number from 10 to 20. c) Cyclic voltammograms of the Fe_3O_4 -MCP electrode and Fe_3O_4 -nonporous Ag electrode for the same bilayer number ($m = 20$) at a scan rate of 5 mV s^{-1} . d) Cycling retention test of the Fe_3O_4 -MCP electrode with a mass loading of 0.88 mg cm^{-2} at a scan rate of 100 mV s^{-1} .

underwent a nearly perfect ligand-exchange reaction with NH_2 -functionalized small TAA molecules during the LbL process, which substantially decreased the interparticle distance between Ag NPs to $\approx 6 \text{ \AA}$. This decreased distance induced the metallic fusion of the multilayered Ag NPs at room temperature without additional treatments. The resultant $(\text{TOAS-Ag NP/TAA})_{20}$ multilayers achieved a remarkably high electrical conductivity of $1.60 \times 10^5 \text{ S cm}^{-1}$ and a low sheet resistance of $0.14 \text{ } \Omega \text{ sq}^{-1}$. Our approach can be widely applied to various substrates, including cellulose papers, polyesters, and cottons, irrespective of substrate size or shape. Furthermore, we confirmed that our highly porous MCPs with large surface areas can be used as conductive reservoirs for high-performance energy-storage electrodes. In particular, $(\text{OA-Fe}_3\text{O}_4 \text{ NP/TAA})_{20}$ multilayer-coated MCP electrodes exhibited a high areal capacitance of 212 mF cm^{-2} (241 F g^{-1}) at a scan rate of 5 mV s^{-1} , which was ten times higher than that of their nonporous equivalent. We believe that our novel metallic fusion-based strategy can be

an important and facile tool for preparing various conductive and soft electrodes for energy-storage applications.

4. Experimental Section

Materials: All chemical reagents for experiments were purchased from Sigma-Aldrich and used without further purifications. Organic solvents, including toluene and ethanol, were purchased from Daejung Chemicals & Metals Co., Ltd. (Republic of Korea).

Synthesis of TOAS-Ag NPs: Tetraoctylammonium thiosulfate-stabilized Ag NPs in toluene were prepared by the modified Brust-Schiffrin method.^[51,52] In brief, 0.9 mmol of silver nitrate (AgNO_3) in deionized water (24 mL) and 2.25 mmol of tetraoctylammonium bromide in toluene (24 mL) were added to a reaction flask and stirred for 10 min at room temperature before 3.6 mmol of sodium thiosulfate was added. The addition of $\text{Na}_2\text{S}_2\text{O}_3$ caused the cloudy mixture solution to be clear. After 10 min, the transparent toluene phase containing silver precursor ions (Ag^+) was transferred to another reaction flask. Next, 1.35 mmol of sodium borohydride, a reducing agent, in deionized water (24 mL)

was added to the toluene solution. As soon as the reducing agent was added, the color of the mixture solution became deep brown, indicating the formation of Ag NPs. The mixture solution was vigorously stirred for 10 min. After that, the deep brown-colored toluene phase was isolated from the mixture solution and successively washed with deionized water, HCl (10 mmol L⁻¹), and NaOH (10 mmol L⁻¹) several times using a separating funnel. The larger TOAS-Ag NPs in size were removed by centrifugation (8000 rpm, 10 min, 20 °C), and finally the TOAS-Ag NPs with ≈8.3 nm in diameter were obtained.

Synthesis of OA-Ag NPs: OA-stabilized Ag NPs in toluene were synthesized as previously reported by Lin et al.^[56] Silver trifluoroacetate (1.8 mmol), oleic acid (11.0 mmol), and isoamyl ether (30 mL) were mixed in a three-neck flask under an argon atmosphere. The reaction mixture was heated to 160 °C at a rate of 1.5 °C min⁻¹ and magnetically stirred at this temperature for 30 min. During the reaction, the mixture solution gradually turned dark brown, which indicated the formation of highly concentrated NPs. After the completion of the reaction, the mixture was cooled to room temperature and centrifuged (5000 rpm, 10 min, 20 °C) with excess ethanol to remove residual impurities, and the resulting OA-Ag NP powder was dispersed in toluene.

Synthesis of OA-Fe₃O₄ NPs: OA-stabilized Fe₃O₄ NPs in toluene were prepared as previously reported by Sun et al.^[57] Iron(III) acetylacetonate (2 mmol), 1,2-hexadecanediol (10 mmol), oleic acid (5 mmol), oleylamine (6 mmol), and benzyl ether (20 mL) were mixed in a three-neck flask and magnetically stirred under a flow of nitrogen. The reaction mixture was heated at 200 °C for 2 h and then heated at 300 °C for 1 h for refluxing. After that, the black-colored mixture was cooled to room temperature and centrifuged (8000 rpm, 10 min, 20 °C) with excess ethanol to eliminate remaining impurities. The black precipitates separated by centrifugations were dissolved in toluene, which contained oleic acid (0.05 mL) and oleylamine (0.05 mL). Any aggregation of NPs was removed by additional centrifugation (6000 rpm, 10 min, 20 °C), and the OA-Fe₃O₄ NPs in toluene were produced.

Assembly of (Organic Ligand-Stabilized NP/TAA)_n Multilayers: Si wafer, quartz glass, PET, and gold-sputtered Si wafer (for FTIR analysis) substrates were irradiated with UV light (λ ≈ 350 nm) for 10 min before the multilayers were deposited. Commercial cellulose paper (Korean Hanji), polyester, and cotton substrates with a lot of hydrophilic groups were used without UV irradiation or chemical treatments. These substrates were dipped into a 1 mg mL⁻¹ of poly(ethylenimine) (branched, M_w ≈ 800) in ethanol for 30 min, washed twice with pure ethanol, and dried under a gentle air stream. The PEI-coated substrates were dipped into a toluene solution of NPs (10 mg mL⁻¹) for 60 min, washed with pure toluene, and thoroughly dried with the air stream. Subsequently, the substrates were dipped into an ethanol solution of TAA (1 mg mL⁻¹) for 20 min. These dipping cycles were repeated until the desired bilayer number was obtained.

Characterization: The structure and crystallinity of NPs were investigated by HR-TEM (Tecnai 20, FEI). X-ray diffraction (XRD) pattern was obtained using XRD-2500/PC (Rigaku) with Cu Kα radiation (40 kV, 150 mA). The surface morphology, film thickness, and EDX of multilayers on substrates were examined by FE-SEM (S-4800, HITACHI). Vibrational spectra of multilayers on gold-sputtered Si wafers were measured by FTIR spectroscopy (CARY 600, Agilent Technologies) in the specular mode at room temperature. The acquired raw data were plotted after baseline corrections, and the final spectra were smoothed using spectrum analyzing software (OMNIC 9, Thermo Scientific). UV-vis absorbance spectra of multilayers on quartz glasses were recorded using Lambda 35 (Perkin Elmer) across a wavelength ranging from 200 to 800 nm. Sheet resistance was examined by the four-probe method using Loresta-GP MCP-T610 (Mitsubishi Chemical Analytech) and electrical conductivity was calculated from the sheet resistance and the film thickness evaluated by cross-sectional FE-SEM images. Temperature-dependent electrical conductivity was measured using physical property measurement system (PPMS-9, Quantum Design) over a temperature range from 2 to 300 K.

Atomistic MD Simulations: All atomistic MD simulations were performed for a model system consisting of TAA molecules sandwiched between Ag atomic surfaces. The initial molecular geometries were prepared by placing TAA molecules between Ag slabs built with a

face-centered cubic stacking arrangement. The face consisted of a 5 × 7 supercell. For this system, isothermal-isobaric system (NPT)-ensemble MD simulations were carried out at 298 K and 1 bar using the COMPASS force field^[58] (COMPASS II) implemented in the Forcite module of Materials Studio package (BIOVIA). Temperature and pressure were kept constant using the Nose-Hoover-Langevin thermostat^[59] and Parrinello-Rahman barostat,^[60] respectively. For all NPT MD runs, the electrostatic potential energy was calculated by the Ewald summation method with an accuracy of 0.1 kcal mol⁻¹ and a buffer width of 0.5 Å, and the van der Waals potential energy was evaluated by the atom-based technique with a cutoff distance of 12.5 Å and a spline width of 1 Å. The MD system was equilibrated for 5 ns with a time step of 1 fs.

Electrochemical Measurements: The electrochemical tests of all electrodes were performed using an Ivium-n-Stat instrument (Ivium Technologies). Individual electrodes were characterized in a three-electrode cell configuration using aqueous Na₂SO₃ (0.5 M) as an electrolyte. An Ag/AgCl electrode saturated by NaCl (3 M) and a platinum wire were used as the reference and counter electrodes, respectively. The active area of working electrodes was fixed at 2 cm². CV and GCD measurements were carried out with potentials ranging from -1 to 0 V. Electrochemical impedance spectroscopy (EIS) measurements were performed in a frequency ranging from 100 kHz to 0.1 Hz with a perturbation amplitude of 0.01 V. The electrochemical capacitance (C), including areal and specific capacitances, was evaluated from CV curves using Equation (1)

$$C = \frac{\int i(v)dv}{2v\Delta VS} \quad (1)$$

where *i*, *v*, and Δ*V* are the current, scan rate (mV s⁻¹), and operating voltage window, respectively. The variable (*S*) corresponds to the active area of working electrodes in areal capacitance, or the mass of active materials in specific capacitance.

Supporting Information

Supporting Information is available from the Wiley Online Library or from the author.

Acknowledgements

Y.S. and D.K. contributed equally to this work. This work was supported by the National Research Foundation of Korea (NRF) grant funded by the Korea government (MSIP; Ministry of Science, ICT & Future Planning) (No. 2018R1A2A1A05019452).

Conflict of Interest

The authors declare no conflict of interest.

Keywords

energy-storage electrodes, flexible electrodes, layer-by-layer assembly, room-temperature metallic fusion, tetraoctylammonium thiosulfate-stabilized silver nanoparticles

Received: September 18, 2018

Revised: February 16, 2019

Published online: April 26, 2019

[1] D.-H. Kim, J.-H. Ahn, W. M. Choi, H.-S. Kim, T.-H. Kim, J. Song, Y. Y. Huang, Z. Liu, C. Lu, J. A. Rogers, *Science* **2008**, 320, 507.

- [2] Y. Kim, J. Zhu, B. Yeom, M. D. Prima, X. Su, J.-G. Kim, S. J. Yoo, C. Uher, N. A. Kotov, *Nature* **2013**, *500*, 59.
- [3] Y. Sun, W. M. Choi, H. Jiang, Y. Y. Huang, J. A. Rogers, *Nat. Nanotechnol.* **2006**, *1*, 201.
- [4] M. K. Choi, J. Yang, K. Kang, D. C. Kim, C. Choi, C. Park, S. J. Kim, S. I. Chae, T.-H. Kim, J. H. Kim, T. Hyeon, D.-H. Kim, *Nat. Commun.* **2015**, *6*, 7149.
- [5] H. Lee, T. K. Choi, Y. B. Lee, H. R. Cho, R. Ghaffari, L. Wang, H. J. Choi, T. D. Chung, N. Lu, T. Hyeon, S. H. Choi, D.-H. Kim, *Nat. Nanotechnol.* **2016**, *11*, 566.
- [6] J. Wang, S. Li, F. Yi, Y. Zi, J. Lin, X. Wang, Y. Xu, Z. L. Wang, *Nat. Commun.* **2016**, *7*, 12744.
- [7] Z. Bao, X. Chen, *Adv. Mater.* **2016**, *28*, 4177.
- [8] Y. Shao, M. F. El-Kady, L. J. Wang, Q. Zhang, Y. Li, H. Wang, M. F. Mousavi, R. B. Kaner, *Chem. Soc. Rev.* **2015**, *44*, 3639.
- [9] X. Peng, L. Peng, C. Wu, Y. Xie, *Chem. Soc. Rev.* **2014**, *43*, 3303.
- [10] S.-Y. Min, Y. Lee, S. H. Kim, C. Park, T.-W. Lee, *ACS Nano* **2017**, *11*, 3681.
- [11] L. Hu, J. W. Choi, Y. Yang, S. Jeong, F. L. Mantia, L.-F. Cui, Y. Cui, *Proc. Natl. Acad. Sci. USA* **2009**, *106*, 21490.
- [12] M. J. Oh, Y. H. Kim, G. H. Choi, A. R. Park, Y. M. Lee, B. Park, C. H. Pang, T.-I. Kim, P. J. Yoo, *Adv. Funct. Mater.* **2016**, *26*, 8726.
- [13] L. Polavarapu, K. K. Manga, H. D. Cao, K. P. Loh, Q.-H. Xu, *Chem. Mater.* **2011**, *23*, 3273.
- [14] F. Xu, Y. Zhu, *Adv. Mater.* **2012**, *24*, 5117.
- [15] S. De, T. M. Higgins, P. E. Lyons, E. M. Doherty, P. N. Nirmalraj, W. J. Blau, J. J. Boland, J. N. Coleman, *ACS Nano* **2009**, *3*, 1767.
- [16] S. J. Lee, Y.-H. Kim, J. K. Kim, H. Baik, J. H. Park, J. Lee, J. Nam, J. H. Park, T.-W. Lee, G.-R. Yi, J. H. Cho, *Nanoscale* **2014**, *6*, 11828.
- [17] H.-S. Ko, Y. Lee, S.-Y. Min, S.-J. Kwon, T.-W. Lee, *Nanoscale* **2017**, *9*, 15766.
- [18] Y. Li, Y. Wu, B. S. Ong, *J. Am. Chem. Soc.* **2005**, *127*, 3266.
- [19] B. T. Anto, S. Sivaramakrishnan, L.-L. Chua, P. K. H. Ho, *Adv. Funct. Mater.* **2010**, *20*, 296.
- [20] S. Magdassi, M. Grouchko, O. Berezin, A. Kamyshny, *ACS Nano* **2010**, *4*, 1943.
- [21] M. Grouchko, A. Kamyshny, C. F. Mihailescu, D. F. Anghel, S. Magdassi, *ACS Nano* **2011**, *5*, 3354.
- [22] Y. Long, J. Wu, H. Wang, X. Zhang, N. Zhao, J. Xu, *J. Mater. Chem.* **2011**, *21*, 4875.
- [23] A. T. Fafarman, S.-H. Hong, S. J. Oh, H. Caglayan, X. Ye, B. T. Diroll, N. Engheta, C. B. Murray, C. R. Kagan, *ACS Nano* **2014**, *8*, 2746.
- [24] J. Perelaer, R. Jani, M. Grouchko, A. Kamyshny, S. Magdassi, U. S. Schubert, *Adv. Mater.* **2012**, *24*, 3993.
- [25] J. Perelaer, P. J. Smith, D. Mager, D. Soltman, S. K. Volkman, V. Subramanian, J. G. Korvink, U. S. Schubert, *J. Mater. Chem.* **2010**, *20*, 8446.
- [26] M. Grouchko, P. Roitman, X. Zhu, I. Popov, A. Kamyshny, H. Su, S. Magdassi, *Nat. Commun.* **2014**, *5*, 2994.
- [27] B. A. Korgel, S. Fullam, S. Connolly, D. Fitzmaurice, *J. Phys. Chem. B* **1998**, *102*, 8379.
- [28] J. N. Israelachvili, *Intermolecular and Surface Forces*, Academic Press, New York **2011**, p. 281.
- [29] L. Yuan, B. Yao, B. Hu, K. Huo, W. Chen, J. Zhou, *Energy Environ. Sci.* **2013**, *6*, 470.
- [30] D. Ge, L. Yang, L. Fan, C. Zhang, X. Xiao, Y. Gogotsi, S. Yang, *Nano Energy* **2015**, *11*, 568.
- [31] L. Hu, Y. Cui, *Energy Environ. Sci.* **2012**, *5*, 6423.
- [32] Y.-Z. Zhang, Y. Wang, T. Cheng, W.-Y. Lai, H. Pang, W. Huang, *Chem. Soc. Rev.* **2015**, *44*, 5181.
- [33] B. Yao, J. Zhang, T. Kou, Y. Song, T. Liu, Y. Li, *Adv. Sci.* **2017**, *4*, 1700107.
- [34] L. Liu, Z. Niu, L. Zhang, W. Zhou, X. Chen, S. Xie, *Adv. Mater.* **2014**, *26*, 4855.
- [35] J. Chen, H. Bi, S. Sun, Y. Tang, W. Zhao, T. Lin, D. Wan, F. Huang, X. Zhou, X. Xie, M. Jiang, *ACS Appl. Mater. Interfaces* **2013**, *5*, 1408.
- [36] G. Decher, *Science* **1997**, *277*, 1232.
- [37] F. Caruso, R. A. Caruso, H. Möhwald, *Science* **1998**, *282*, 1111.
- [38] S. S. Shiratori, M. F. Rubner, *Macromolecules* **2000**, *33*, 4213.
- [39] P. Podsiadlo, A. K. Kaushik, E. M. Arruda, A. M. Waas, B. S. Shim, J. Xu, H. Nandivada, B. G. Pumplin, J. Lahann, A. Ramamoorthy, N. A. Kotov, *Science* **2007**, *318*, 80.
- [40] K. E. Tetty, J. W. C. Ho, D. Lee, *J. Phys. Chem. C* **2011**, *115*, 6297.
- [41] S. W. Lee, N. Yabuuchi, B. M. Gallant, S. Chen, B.-S. Kim, P. T. Hammond, Y. Shao-Horn, *Nat. Nanotechnol.* **2010**, *5*, 531.
- [42] S. Y. Kim, J. Hong, R. Kavian, S. W. Lee, M. N. Hyder, Y. Shao-Horn, P. T. Hammond, *Energy Environ. Sci.* **2013**, *6*, 888.
- [43] J. Cho, K. Char, J.-D. Hong, K.-B. Lee, *Adv. Mater.* **2001**, *13*, 1076.
- [44] J.-S. Lee, J. Cho, C. Lee, I. Kim, J. Park, Y.-M. Kim, H. Shin, J. Lee, F. Caruso, *Nat. Nanotechnol.* **2007**, *2*, 790.
- [45] Y. Ko, H. Baek, Y. Kim, M. Yoon, J. Cho, *ACS Nano* **2013**, *7*, 143.
- [46] D. Kim, S. Cheong, Y. G. Ahn, S. W. Ryu, J.-K. Kim, J. Cho, *Nanoscale* **2016**, *8*, 7000.
- [47] A. G. Dong, Y. J. Wang, Y. Tang, N. Ren, W. L. Yang, Z. Gao, *Chem. Commun.* **2002**, *0*, 350.
- [48] M. Yang, Y. Yang, H. Yang, G. Shen, R. Yu, *Biomaterials* **2006**, *27*, 246.
- [49] J. Schmitt, G. Decher, W. J. Dressick, S. L. Brandow, R. E. Geer, R. Shashidhar, J. M. Calvert, *Adv. Mater.* **1997**, *9*, 61.
- [50] Y. Cho, W. Lee, Y. K. Jhon, J. Genzer, K. Char, *Small* **2010**, *6*, 2683.
- [51] M. Brust, M. Walker, D. Bethell, D. J. Schiffrin, R. Whyman, *J. Chem. Soc., Chem. Commun.* **1994**, *0*, 801.
- [52] S. R. Isaacs, E. C. Cutler, J.-S. Park, T. R. Lee, Y.-S. Shon, *Langmuir* **2005**, *21*, 5689.
- [53] C. L. Doolittle, M. J. McLaughlin, J. K. Kirby, D. A. Navarro, *J. Hazard. Mater.* **2015**, *300*, 788.
- [54] F. J. Ibañez, F. P. Zamborini, *ACS Nano* **2008**, *2*, 1543.
- [55] J. Mu, B. Chen, Z. Guo, M. Zhang, Z. Zhang, P. Zhang, C. Shao, Y. Liu, *Nanoscale* **2011**, *3*, 5034.
- [56] X. Z. Lin, X. Teng, H. Yang, *Langmuir* **2003**, *19*, 10081.
- [57] S. Sun, H. Zeng, D. B. Robinson, S. Raoux, P. M. Rice, S. X. Wang, G. Li, *J. Am. Chem. Soc.* **2004**, *126*, 273.
- [58] H. Sun, *J. Phys. Chem. B* **1998**, *102*, 7338.
- [59] A. A. Samoletov, C. P. Dettmann, M. A. J. Chaplain, *J. Stat. Phys.* **2007**, *128*, 1321.
- [60] M. Parrinello, A. Rahman, *J. Appl. Phys.* **1981**, *52*, 7182.